SYNTHETIC BIOLOGY

Metal ion–regulated assembly of designed modular protein cages

Jana Aupič[1]†, Fabio Lapenta[1,2]‡, Žiga Strmšek[1], Estera Merljak[1,3], Tjaša Plaper[1,3], Roman Jerala[1,2]*

Coiled-coil (CC) dimers are versatile, customizable building modules for the design of diverse protein architectures unknown in nature. Incorporation of dynamic self-assembly, regulated by a selected chemical signal, represents an important challenge in the construction of functional polypeptide nanostructures. Here, we engineered metal binding sites to render an orthogonal set of CC heterodimers Zn(II)-responsive as a generally applicable principle. The designed peptides assemble into CC heterodimers only in the presence of Zn(II) ions, reversibly dissociate by metal ion sequestration, and additionally act as pH switches, with low pH triggering disassembly. The developed Zn(II)-responsive CC set is used to construct programmable folding of CC-based nanostructures, from protein triangles to a two-chain bipyramidal protein cage that closes and opens depending on the metal ion. This demonstrates that dynamic self-assembly can be designed into CC-based protein cages by incorporation of metal ion–responsive CC building modules that act as conformational switches and that could also be used in other contexts.

INTRODUCTION

Metal ion binding is integral for function, folding, and formation of quaternary complexes of many proteins (*1*, *2*). Understanding metal-protein interactions is, therefore, an important piece of the protein folding puzzle. Because metal coordination can be easily regulated via changes in the concentration of a competing chelator or pH, metal ion binding and unbinding events often trigger conformational changes, a cornerstone of many natural regulatory mechanisms. Conformational changes induced by metal ion binding regulate muscle contraction (*3*), ion channel flux (*4*), DNA binding affinity of transcription factors (*5*–*7*), and mediate ubiquitination (*8*). Designing metal binding sites into protein scaffolds is, therefore, an attractive strategy toward achieving designed protein complexes with externally controllable assembly/disassembly, mimicking natural molecular machines.

Coiled coils (CCs) have been proven to be suitable building blocks for designing modular protein nanostructures (*9*–*11*). CC sequences are characterized by a heptad repeat pattern, commonly denoted as *abcdefg*, where hydrophobic residues are located at positions *a* and *d*, while other positions are predominantly occupied by polar amino acid residues (*12*). Assembly of individual peptide chains into a left-handed superhelix is mediated by hydrophobic interactions between amino acid residues at *a* and *d* positions, and salt bridging between residues at *e* and *g* positions. Residues at *b*, *c*, and *f* positions primarily do not affect oligomerization properties but contribute to the thermodynamic stability of the CC assembly (*13*). Thanks to the insights into the rules governing the sequence-structure relationship in CCs, it is feasible to precisely design the number and the orientation of α helices in a CC assembly by carefully selecting interacting residues (*14*).

By correctly combining CC-forming peptides or linking them to other oligomerizing units, diverse CC-based nanostructures can be created (*9*–*11*). We have previously shown that CC dimers can be used to design mono- and multimeric protein cages of different polyhedral shapes (*15*–*19*). This strategy, termed CC protein origami (CCPO), is based on the concatenation of orthogonal CC-forming peptides (*20*) into one or several polypeptide chains that self-assemble into the desired fold determined by the pattern of pairwise interactions between the CC-forming modules.

That CCs can also be engineered to bind metal ions with high selectivity and affinity has been first demonstrated more than three decades ago (*21*, *22*). Initial design attempts focused on Zn(II) binding sites; however, subsequent work has shown CCs can be adapted to bind a diverse array of metal ions (*23*–*27*). Moreover, multiple structurally diverse binding sites could be incorporated into a single-peptide scaffold (*28*–*30*), with some designs mimicking natural metalloenzymes both in structure and function (*31*, *32*). Because metal binding can be coupled to protein folding and assembly, many of the hitherto designed metal binding peptides assumed a well-folded structure only in the presence of metal ions (*22*, *33*–*35*), in effect acting as metal-regulated conformational switches. The designs reported so far were based, with few exceptions (*36*, *37*), not on CC dimers but on CC trimers and higher-order α-helical bundles with metal ions buried in the cavity between multiple helices. Recently, we demonstrated that a monomeric peptide could be transformed into a conformational switch by incorporating a His residue at the *e* position in its final heptad (*34*). The peptide, named SwitCCh, formed a parallel CC homodimer only in the presence of Zn(II) ions. While CCs and α-helical bundles can act as conformational switches individually, they could also be applied to program conformational flexibility and regulated self-assembly into larger protein nanostructures. For example, it has been recently shown in a study by Tezcan and co-workers that four-helix bundles can serve as building blocks for designing larger cage-like architectures with metal-mediated assembly (*38*). Similarly, by incorporating Zn(II)-dependent CC dimers into CCPO cages, it might be possible to reversibly regulate their folding and (dis)assembly.

[1]Department of Synthetic Biology and Immunology, National Institute of Chemistry, Hajdrihova 19, SI-1000 Ljubljana, Slovenia. [2]EN-FIST Centre of Excellence, Trg OF 13, SI-1000 Ljubljana, Slovenia. [3]Interdisciplinary Doctoral Programme in Biomedicine, University of Ljubljana, Kongresni trg 12, SI-1000 Ljubljana, Slovenia.
*Corresponding author. Email: roman.jerala@ki.si
†Present address: National Research Council of Italy Institute of Materials (CNR-IOM) C/o SISSA, Via Bonomea 265, 34136 Trieste, Italy.
‡Present address: Laboratory of Environmental and Life Sciences, University of Nova Gorica, Vipavska cesta 13, SI-5000 Nova Gorica, Slovenia.

Here, we use rational metal-site engineering to design a four-member set of orthogonal Zn(II)-dependent heterodimeric CCs. The designed set is applied to construct single-chain CCPO triangular folds with dynamic Zn(II)-dependent folding. Comparing different design variants, we show that the temperature where Zn(II) ions have a substantial effect on the secondary and tertiary structure can be fine-tuned by CC building block selection and rational mutation of residues at *b*, *c*, and *f* heptad positions. Last, we demonstrate the design of a metal ion–regulated self-assembly of a multimeric CC-based bipyramidal protein cage.

RESULTS

Design of Zn(II)- and pH-responsive CC modules

Most of the hitherto designed orthogonal CC sets are composed of heterodimeric pairs, due to clear design rules for their creation (*39*). Here, we used the orthogonal peptide pairs P3:P4, P5:P6, and P7:P8 from the NICP CC toolkit (*20*) as scaffolds for the design of orthogonal Zn(II)-responsive CC heterodimers. Orthogonality was encoded into the original set by strategically matching polar Asn residues at different *a* heptad positions and by using different charge patterns of Glu and Lys residues at *e* and *g* positions (*20*). The metal binding sites were designed to closely mimic their natural counterparts. In natural proteins, Zn(II) ions are predominantly coordinated by four or three tetrahedrally arranged amino acid residues, most frequently Cys and His, with the average distance between Zn(II) and the coordinating atom of approximately 2 Å (*40*, *41*). Accordingly, we introduced three His residues into each peptide pair: two into the first peptide and one His residue into the second peptide (Fig. 1, A to D, and table S1). His residues were placed at one of the interacting *d* positions in each pair, where they replaced the dimerization promoting Ile residue, therefore destabilizing peptide

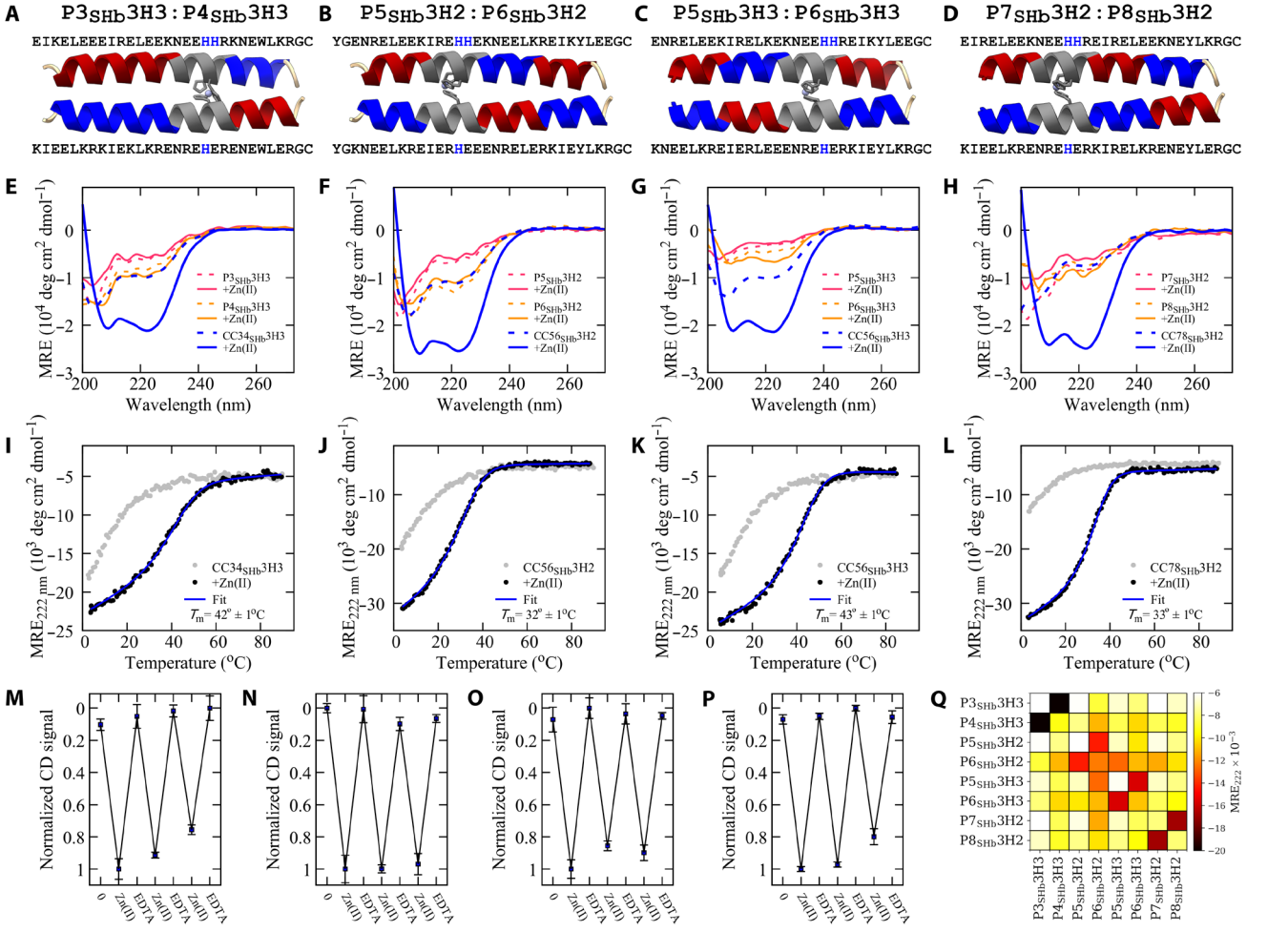

Fig. 1. Design and biophysical characterization of the Zn(II)-responsive orthogonal dimeric CC set. (**A** to **D**) Sequence and design models for $CC34_{SHb}3H3$ (A), $CC56_{SHb}3H2$ (B), $CC56_{SHb}3H3$ (C), and $CC78_{SHb}3H2$ (D). Heptads with negatively and positively charged residues at *e*:*g* positions are colored red and blue, respectively, while heptads containing the $ZnHis_3$ motif are shown in gray. Model CC structures were built with the ISAMBARD software package (*51*). (**E** to **H**) CD spectra in the absence and presence (200 μM) of Zn(II) ions for individual peptides and peptide pair mixtures (20 μM). CD signal is shown as mean residue ellipticity (MRE). (**I** to **L**) MRE at 222 nm as a function of temperature in the presence and absence of Zn(II) ions. Experimental data (dots) were fit with a thermodynamic two-state model (blue line) to determine the melting temperatures (T_m). (**M** to **P**) Normalized CD signal at 222 nm (gray bars) after consecutive additions of equimolar amounts of Zn(II) and EDTA for $CC34_{SHb}3H3$ (M), $CC56_{SHb}3H2$ (N), $CC56_{SHb}3H3$ (O), and $CC78_{SHb}3H2$ (P). The data are shown as means ± SD ($n = 3$). (**Q**) Protein-protein interaction matrix in the presence of Zn(II) ions. Propensity for interaction was estimated from MRE at 222 nm.

interaction in the absence of Zn(II) (fig. S1). In each pair, one of the peptides contained an additional His at a neighboring *e* position to achieve tighter Zn(II) binding, because the homodimeric peptide SwitCCh, where coordination was mediated by only two His residues, displayed a relatively low Zn(II) binding affinity [dissociation constant (K_d) ~ 400 μM] (*34*). To probe the effect of binding site placement within the four-heptad peptide on conformational switching, we positioned the $ZnHis_3$ motif into the second [$CC56_{SHb}3H2$ (Fig. 1B) and $CC78_{SHb}3H2$ (Fig. 1D)], third [$CC34_{SHb}3H3$ (Fig. 1A) and $CC56_{SHb}3H3$ (Fig. 1C)], or fourth heptad [$CC34_{SHb}3H4$ (table S1)]. In addition, residues at the *b*, *c*, *f* heptad positions were modified to promote salt bridging, thus increasing α-helical propensity and stability (*13*). Last, we created model structures of designed peptide pairs with ISAMBARD to confirm His residues were at an appropriate distance for Zn(II) coordination (Fig. 1, A to D).

The secondary structure of the designed peptide pairs was analyzed using circular dichroism (CD) spectroscopy (Fig. 1, E to H). In the absence of metal ions, the peptide pairs were predominantly unfolded with the exception of $CC34_{SHb}3H4$ that contained the Zn(II) binding site in the fourth heptad, close to the C-terminal end (fig. S2). Peptide pair $CC34_{SHb}3H4$ was, therefore, not examined further. For other peptide pairs, the addition of Zn(II) ions resulted in a large increase in ellipticity at 208 and 222 nm, characteristic for the formation of helical structures (Fig. 1, E to H). To confirm the observed increase in helicity was not due to the formation of homo-oligomeric species, individual peptides were investigated. No Zn(II)-dependent changes in secondary structure were observed, confirming that both peptide partners were needed for the formation of α-helical CCs. In addition, CD spectroscopy was used to monitor temperature-induced unfolding (Fig. 1, I to L). In the absence of Zn(II) ions, melting temperatures (T_m) were below 20°C. Addition of Zn(II) ions caused a large increase in T_m. Notably, peptide pairs $CC34_{SHb}3H3$ (Fig. 1I) and $CC56_{SHb}3H3$ (Fig. 1K) with the $ZnHis_3$ site in the third heptad were characterized by a higher T_m (42° to 43°C) than peptide pairs $CC56_{SHb}3H2$ (Fig. 1J) and $CC78_{SHb}3H2$ (Fig. 1L; T_m = 32° to 33°C), where the binding site was located in the second heptad in the center of the peptide.

Next, we used size exclusion chromatography coupled to multi-angle light scattering (SEC-MALS) to confirm that Zn(II) ions induced formation of CC dimers rather than higher-order species. In the absence of Zn(II) ions, we observed two peaks in the chromatograms of peptide mixtures, corresponding to individual peptides (fig. S3). Addition of Zn(II) ions to the mobile phase resulted in peptide pairs eluting in a single peak whose mass corresponded to a dimer as designed (fig. S4).

Zn(II) binding affinity was determined by monitoring ellipticity at 222 nm as a function of Zn(II) concentration (figs. S5 and S6). For all peptide pairs, ellipticity increased until Zn(II):CC molar ratio was approximately 1:1, after which saturation was observed. This indicated a single Zn(II) ion bound into each designed heterodimer. K_ds, calculated by fitting a two-state model to experimental data (see the Supplementary Methods), were in the low micromolar region with Zn(II) binding strongest to $CC34_{SHb}3H3$ (K_d = 1 ± 0.1 μM). We observed CC formation also after the addition of other divalent metal ions [Ni(II), Co(II), and Cu(II)]; however, the K_ds were 10- to 300-fold higher (figs. S7 to S9).

Next, we examined whether metal-induced self-assembly could be reversed either by the addition of a strong metal chelator such as EDTA or by decreasing the pH, which affects the protonation state and coordination ability of His residues. Upon EDTA addition, the CCs promptly disassembled, reflected in the decrease in ellipticity at 222 nm to levels observed before Zn(II) addition (Fig. 1, M to P). Moreover, switching between the monomer and dimer state could be repeated reversibly for several cycles, without loss in amplitude. In addition, all four peptide pairs exhibited pH-induced disassembly at low pH (fig. S10). For designs $CC56_{SHb}3H2$ and $CC78_{SHb}3H2$, the transition was highly cooperative with a midpoint at pH 6, while for $CC34_{SHb}3H3$ and $CC56_{SHb}3H3$, dissociation occurred over a broader range of pH values with a midpoint at pH ~5. The reduced cooperativity and lower transition pH values are most likely due to the stronger association between peptide chains as reflected in thermal stability, making His residues more resistant to protonation.

If the designed Zn(II)-dependent CCs were to be used for the construction of modular CC nanostructures, they ought to display high interaction specificity (Fig. 1Q). Pairwise all-by-all CD analysis revealed each peptide formed a CC preferentially with its peptide partner. Some cross-reactivity was observed at higher Zn(II) concentrations. While peptide $P6_{SHb}3H3$ still preferentially bound its partner $P5_{SHb}3H3$, it displayed a homo-oligomerizing tendency and weakly interacted with peptides $P6_{SHb}3H2$ and $P4_{SHb}3H3$ (fig. S11).

To further probe the modularity of the binding site design, we examined whether inserting the $ZnHis_3$ motif into the second and third heptads of $CC56_{SHb}$ would result in a CC able to bind two Zn(II) ions (table S1). While the resulting module $CC56_{SHb}6H$ was unresponsive to Zn(II) ions, the individual peptide $P6_{SHb}6H$ displayed homo-oligomerization in response to Zn(II) ions at high peptide concentrations (fig. S12), indicating that insertion of a larger number of mutations results in less predictable CC pairing.

Tunable Zn(II)-driven regulation of CCPO self-assembly

Because the development of synthetic protein cages and materials with controllable and reversible self-assembly is one of the current goals of protein design, we sought to use the Zn(II)-responsive CCs to construct single-chain CCPO cages with inducible folding and unfolding. As a case study, we used a triangular fold composed of six peptide modules (Fig. 2 and table S2). The control construct TRI6-control (Fig. 2A), composed of peptide pairs $CC34_{SHb}$, $CC56_{SHb}$, and $CC78_{SHb}$ without Zn(II) binding sites, showed high helicity (~75%; Fig. 2B) and high thermal stability (T_m = 82°C; Fig. 2C). CC building blocks were then replaced with their Zn(II)-responsive counterparts: $CC34_{SHb}3H3$, $CC56_{SHb}3H3$, and $CC78_{SHb}3H2$. At 20°C, the resulting design TRI6-1 (Fig. 2D) displayed a high α-helical content (82%) that was independent of Zn(II) ion concentration (Fig. 2, E and F, and fig. S13). Next, we used SEC-MALS to qualitatively evaluate the effect of Zn(II) ions on the tertiary structure. In the absence of metal species, TRI6-1 eluted at approximately the same retention time as the control assembly, indicating that the design assumed a folded triangular state (Fig. 2G). Addition of Zn(II) had a minimal effect on the retention time. Nonetheless, thermal denaturation measurements revealed addition of Zn(II) ions significantly increased the protein's thermal stability, with T_m increasing from 37° ± 1°C to 56° ± 1°C (Fig. 2F). Zn(II) ions had the highest impact on secondary structure at ~50°C, triggering a transition from the unfolded to the folded state (Fig. 2H). Together, the results show that while the insertion of the $ZnHis_3$ binding site into each CC module did not prevent the formation of the triangular fold in the absence of Zn(II) ions, it did diminish its stability, which could however be partially recovered by the addition of Zn(II) ions.

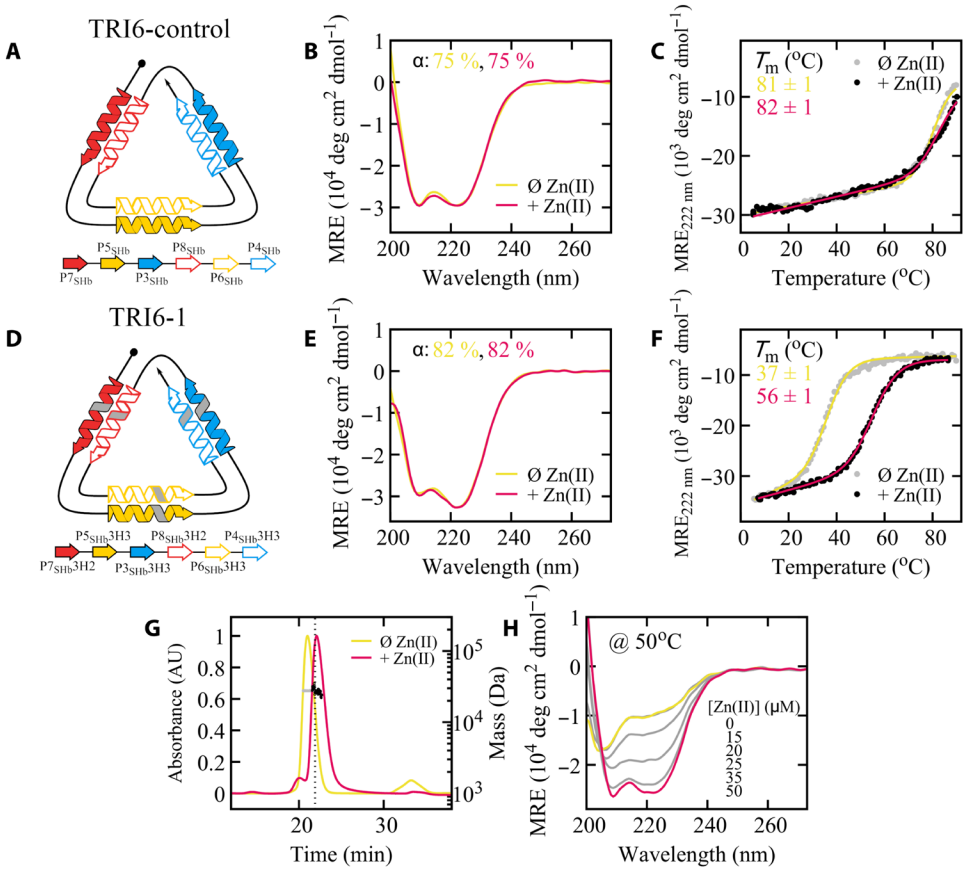

Fig. 2. Biophysical characterization of a Zn(II)-responsive CCPO triangle. (**A**) Schematic representation of the CCPO triangle design TRI6-control along with the arrangement of CC building blocks. (**B**) MRE as a function of wavelength in the absence and presence of Zn(II) ions (yellow and red curves, respectively) observed for TRI6-control. (**C**) MRE at 222 nm as a function of temperature in the absence and presence of Zn(II) ions (gray and black dots, respectively) observed for TRI6-control. A two-state unfolding model was fit to experimental data (yellow and red curves, respectively) to determine the T_ms. (**D**) Schematic representation of the CCPO triangle design TRI6-1. (**E**) MRE as a function of wavelength in the absence and presence of Zn(II) ions (yellow and red curves, respectively) observed for TRI6-1. (**F**) MRE at 222 nm as a function of temperature in the absence and presence of Zn(II) ions (gray and black dots, respectively) observed for TRI6-1. T_m was determined by fitting a two-state unfolding model to experimental data (yellow and red curves, respectively). (**G**) SEC-MALS was used to analyze the effect of Zn(II) ions on the tertiary structure of TRI6-1. The dotted line marks the retention time observed for the control construct. (**H**) CD spectra of TRI6-1 at different Zn(II) ion concentrations observed at 50°C. CD profile before the addition of Zn(II) ions is shown in yellow, while the red curve corresponds to the CD profile observed at the highest Zn(II) concentration.

To shift the temperature where Zn(II) ions control protein folding to a lower temperature range, we investigated several alternative CCPO triangle designs, differing in CC building block composition (Fig. 3, A and B, and figs. S13 and S14). After replacing the C-terminal pair $CC34_{SHb}3H3$ with the homodimeric SwitCCh (*34*) (design TRI6-2) and the central building block with $CC56_{SHb}6H$ or the homo-oligomeric $P6_{SHb}6H$ (designs TRI6-3 and TRI6-4, respectively), Zn(II)-dependent folding was observed at 37°C (Fig. 3, C to E, and fig. S14). We further destabilized the triangular fold by modifying *b*, *c*, *f* residues in the N-terminal CC module $CC78_{SHb}3H2$ (*13*). In the construct TRI6-5, we changed all *b*, *c*, *f* residues to Ala, whereas the design TRI6-6 contained in those positions polar negatively charged residues (Fig. 3B). At room temperature, TRI6-5 displayed only low helicity (36%), while TRI6-6 was unfolded (Fig. 3E). In both cases, the addition of Zn(II) led to an increase in helicity (59 and 42%, respectively) and a cooperative unfolding transition at 46° ± 1°C and 27° ± 1°C, respectively (Fig. 3, C and D). Greater degree of unfolding in the absence of Zn(II) ions was also confirmed by SEC-MALS measurements (fig. S14).

To study the effect of Zn(II) ions on the tertiary structure of selected triangular designs (fig. S15) in detail, we used small-angle x-ray scattering (SAXS), which is particularly suitable to study dynamic assemblies. The scattering curve of the control construct (TRI6-control) matched well to a triangular model structure and was characterized by a radius of gyration (R_g) of 2.85 ± 0.05 nm (Fig. 4, A and B), and a maximal particle distance (D_{max}) of 9.7 ± 0.5 nm, in agreement with the design (Fig. 4C). For TRI6-3, TRI6-4, TRI6-5, and TRI6-6, we observed higher D_{max} and R_g values in the absence of Zn(II) (Fig. 4C). In comparison to TRI6-control, TRI6-6 was characterized by a twofold higher D_{max} (21 ± 1 nm), a size increase consistent with unfolding of a monomeric protein (*42*). Kratky analysis further corroborated TRI6-control was well folded and contained multiple domains connected with flexible linkers, while other proteins were either partially or fully unfolded in the absence of Zn(II) ions (Fig. 4D). We evaluated the degree of unfolding in the absence of Zn(II) ions by the ensemble optimization method (EOM) (*43*). Briefly, a large pool of unfolded random chain configurations was generated, after which a genetic algorithm was used to

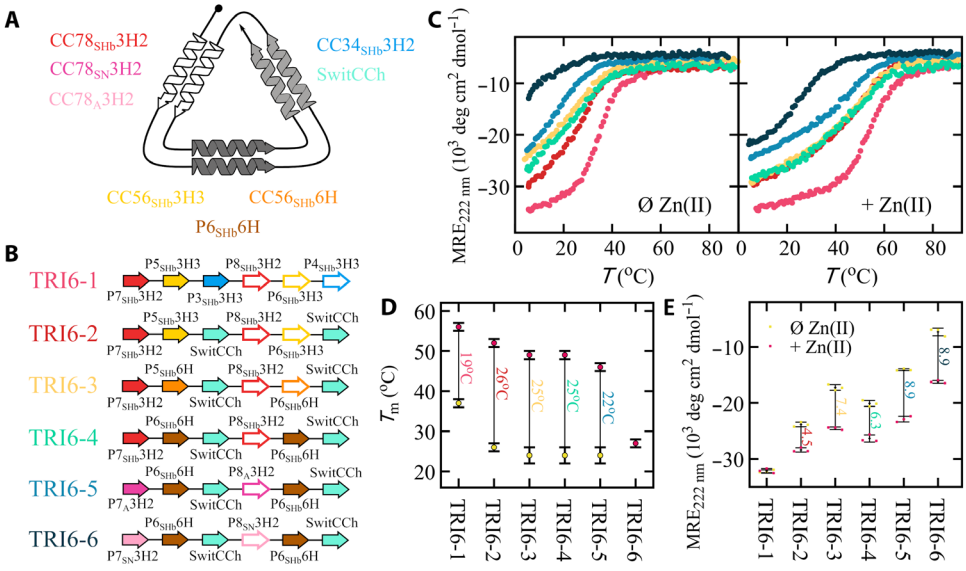

Fig. 3. Modulation of the response of the CCPO triangle to Zn(II) through building block selection. (**A**) Schematic representation of the CCPO triangle design variants along with a list of CC building blocks tested at each edge. (**B**) Arrangement of the peptide segments in the polypeptide chain for each design. (**C**) MRE at 222 nm as a function of temperature (*T*) in the absence (left) and presence (right) of Zn(II) ions. The color coding is as shown in (B). (**D**) T_m in the absence (yellow dots) and presence (red dots) of Zn(II) ions for all designs. T_ms were determined by fitting a two-state unfolding model to experimental data. The error bars depict the uncertainty of the fit. (**E**) Effect of Zn(II) addition on MRE at 222 nm at 20°C. Data are shown as means ± SD ($n = 3$). Individual measurements are shown with yellow and red dots and correspond to MRE observed in the absence and presence of Zn(II) ions, respectively.

select the ensemble of structures best matching the observed SAXS profile (fig. S16). Comparison of R_g distributions calculated from the optimized ensembles indicated only TRI6-6 was completely unfolded in the absence of Zn(II) ions, while other designs were characterized by a more compact ensemble of structures (figs. S16 and S17). We repeated the SAXS measurements at different Zn(II) ion concentrations. Addition of Zn(II) ions led to a well-defined maximum at $qR_g = \sqrt{3}$ in the Kratky spectrum coupled with a decrease in the plateau at higher qR_g values, which indicates that the proteins acquired a more compact fold (Fig. 4D) (*44*). Furthermore, R_g values decreased as Zn(II) concentration was increased (Fig. 4E). At higher Zn(II) concentrations, R_g for TRI6-3, TRI6-4, and TRI6-6 showed a good agreement to the R_g observed for the TRI6-control. The most pronounced change was observed for TRI6-6, which underwent a decrease in R_g from 4.8 ± 0.2 nm to 3.0 ± 0.1 nm. Moreover, SAXS profiles at high Zn(II) concentration were similar to that observed for TRI6-control (fig. S18), particularly in the case of TRI6-4 and TRI6-6, suggesting these constructs assumed a triangular shape (fig. S19).

To support the results of SAXS analysis, folding of TRI6-5 and TRI6-6 was additionally monitored by Förster resonance energy transfer (FRET). Because the N and C termini should come in close proximity as the proteins fold, a pair of cyanine dyes (sulfo-Cy3 and sulfo-Cy5) was attached at the termini, and the FRET ratio was monitored as a function of Zn(II) ion concentration (Fig. 4F). For both designs, increasing the concentration of Zn(II) ions led to a notable rise in the FRET signal, indicating the distance between the N and C termini decreased as the proteins folded, further corroborating the designs assumed a triangular structure in the folded state. To extract binding affinities for CC building blocks, a global fit to FRET titration curves was performed (see the Supplementary Methods). K_d values obtained for modules $P6_{SHb}6H$ and SwitCCh were in the low micromolar region (3 and 10 μM, respectively). Notably, changing *b*, *c*, *f* sites to negatively charged amino acids resulted in a K_d increase of approximately two orders of magnitude from 20 nM for module $CC78_{A\text{-}SHb}3H2$ to 6 μM for $CC78_{SN\text{-}SHb}3H2$. In addition, we showed the triangular structures could be reversibly folded and unfolded by sequestering Zn(II) ions from solution by EDTA addition (fig. S20). Moreover, the addition of other divalent metal ions did not result in a FRET increase, indicating the designs selectively bind Zn(II) ions (fig. S21).

Metal ion–regulated assembly of a heterodimeric CCPO bipyramid

Last, we examined whether the Zn(II)-dependent CCs could be used to reversibly control the assembly process of multimeric CCPO cages. As a proof of concept, we used the recently described heterodimeric CCPO bipyramid $SBP12_{9,b}$ (*17*), composed of two tetrahedrally shaped domains that interact via a triangular interface encompassing three CC dimer–forming peptide segments. We have previously shown that the assembly of the two-chain protein bipyramid could be regulated by proteolysis; however, that process was unidirectional. Aiming to achieve a reversible, Zn(II)-regulated self-assembly, we replaced the interfacing CCs with $CC56_{SHb}3H2$, $CC56_{SHb}3H3$, and $CC78_{SHb}3H2$, while keeping the rest of the modules unchanged (Fig. 5A and table S2). We named the resulting proteins $SBP^{Zn}1$ and $SBP^{Zn}2$ and produced them in *Escherichia coli* (fig. S22).

We first analyzed the assembly of the two tetrahedral domains by CD spectroscopy. Adding Zn(II) ions to an equimolar mixture of $SBP^{Zn}1$ and $SBP^{Zn}2$ increased the α-helical content by 13% (Fig. 5B) and the T_m of the first unfolding transition by 5°C (Fig. 5C). This suggests Zn(II) ions provided additional structural stabilization, most likely to the interfacial segments. SEC-MALS measurements

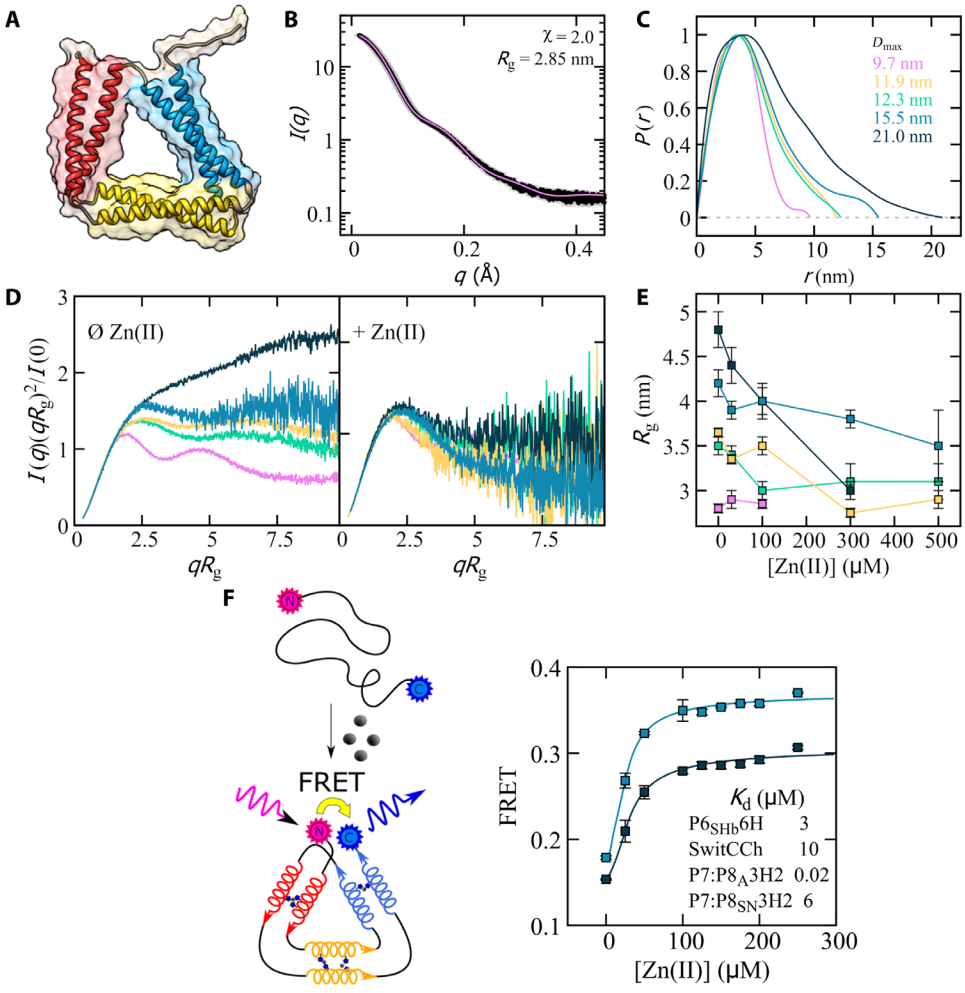

Fig. 4. Structural analysis of the Zn(II)-dependent folding of CCPO triangles with SAXS. (**A**) A molecular model of TRI6-control. (**B**) Scattering intensity $I(q)$ as a function of the scattering vector q. R_g was 2.85 ± 0.02 nm. Scattering profile for TRI6-control (black dots) was in good agreement ($\chi = 2$) with the theoretical scattering (violet curve) calculated from a triangular structure shown in (A). (**C**) Pair distance (r) distribution function $P(r)$ for TRI6-control (violet curve), TRI6-3 (yellow curve), TRI6-4 (green curve), TRI6-5 (blue curve), and TRI6-6 (dark blue curve) in the absence of Zn(II). The same color scheme is applied in each subsequent panel. (**D**) The addition of Zn(II) ions led to large changes in Kratky plots of all designs, demonstrating a transition to more folded structures. (**E**) R_g decreased with increasing Zn(II) concentration. Error bars represent uncertainty in R_g determination. (**F**) Folding of TRI6-5 and TRI6-6 was monitored through Förster resonance energy transfer (FRET) between a pair of terminally attached cyanine dyes. Global thermodynamic model fitting (solid curves) was used to determine the K_ds for Zn(II) ion binding to individual CC building blocks. Data are shown as means ± SD ($n = 3$).

confirmed the tetrahedral domains assembled into a heterodimer only in the presence of Zn(II) ions and were otherwise monomeric (Fig. 5D). On the other hand, secondary structure, thermal stability, and oligomerization state of each individual domain were not significantly affected by Zn(II) ion addition (fig. S23). Next, we labeled the tetrahedral domains at the interface with fluorescent dyes sulfo-Cy3 and sulfo-Cy5 and monitored their association through FRET (Fig. 5E). The addition of Zn(II) caused a strong increase in the FRET signal. Although three binding sites were present at the interacting interface, the plateau was observed after the addition of two equivalents of Zn(II), indicating the binding of two metal ions was sufficient to assemble the bipyramidal cage, as would be expected for two rigidly interacting tetrahedra. Experimental data were fit to a model that described the binding sites as identical (to avoid overfitting) but allowed for cooperativity (see the Supplementary Methods). The determined K_ds were in the nanomolar range ($K_d^1 = 90 \pm 10$ nM, $K_d^2 = 10 \pm 2$ nM). Last, we examined the reversibility of the self-assembly (Fig. 5F). The addition of EDTA to the solution of the SBP^{Zn}1:SBP^{Zn}2-Zn(II) complex led to a decrease in the FRET signal, indicating a disassembly of the bipyramidal cage. Moreover, Zn(II)/EDTA-triggered cycling between the assembled and disassembled state could be performed several times without a substantial loss in the amplitude of the FRET signal. Only weak association was observed in the presence of other divalent metal ions (fig. S24).

To confirm the heterodimer assumed a bipyramidal shape in solution, we analyzed it with SEC-SAXS (Fig. 5G and fig. S25). R_g and D_{max} were 4.2 ± 0.05 nm and 12.3 ± 0.5 nm, respectively, in agreement with values observed for the previously designed two-chain CCPO bipyramid (4.0 and 11.8 nm, respectively) (*17*). To investigate the possible conformational heterogeneity, an ensemble of bipyramidal cage models was compared to the scattering profile. A good fit was obtained with a single bipyramidal cage model,

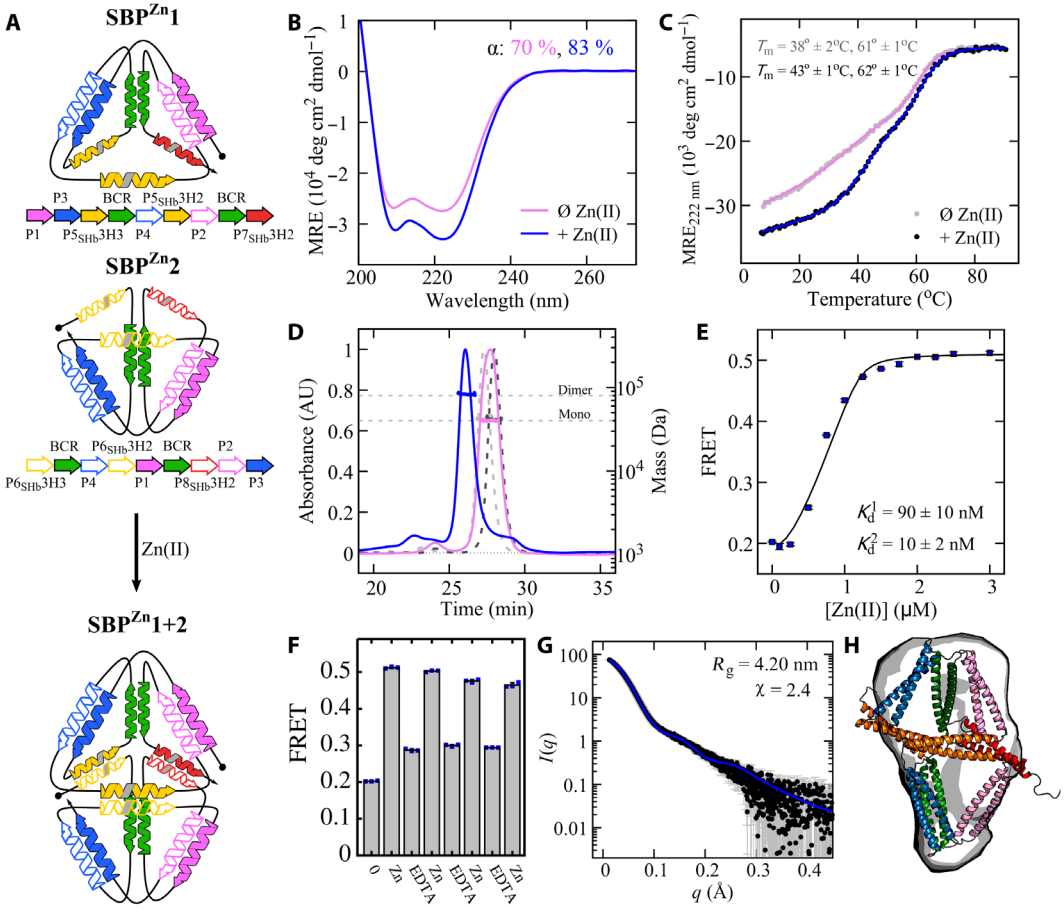

Fig. 5. Design and characterization of Zn(II)-responsive self-assembly of the heterodimeric bipyramidal protein cage. (**A**) Schematic of the designed heterodimeric bipyramidal cage with Zn(II)-dependent self-assembly. (**B**) MRE as a function of wavelength observed for the $SBP^{Zn}1$:$SBP^{Zn}2$ complex in the absence and presence of Zn(II) ions. (**C**) MRE at 222 nm as a function of temperature in the absence (gray dots) and presence (black dots) of Zn(II) ions. (**D**) SEC-MALS demonstrated that $SBP^{Zn}1$ and $SBP^{Zn}2$ assembled into a heterodimer only in the presence of Zn(II) ions (blue curve). The violet curve shows the elution profile of the equimolar $SBP^{Zn}1$:$SBP^{Zn}2$ mixture in the absence of Zn(II), while dashed lines correspond to individual subunits. (**E**) Self-assembly of tetrahedral subunits as a function of Zn(II) ions concentration monitored by FRET (blue symbols). Thermodynamic model fitting (black curve) was used to determine K_ds. Data are shown as means ± SD ($n = 3$). Error bars are smaller than data points. (**F**) Reversible control of the assembly/disassembly with external stimuli. Data are shown as means ± SD ($n = 3$). Blue symbols represent results of individual measurements. (**G**) Scattering intensity $I(q)$ as a function of the scattering vector q. The SAXS profile (black dots) fit well to a single bipyramidal cage model structure (blue curve) shown in (**H**). The fit was evaluated using the chi metric (χ). R_g was comparable to the previously reported bipyramidal cage design $SBP12_{9\_b}$. Data are shown as means ± SD ($n = 40$). (H) Best-fit model of the complex $SBP^{Zn}1$:$SBP^{Zn}2$ superimposed to the molecular envelope reconstructed from SAXS data using ab initio modeling. The molecular envelope was obtained by refining the averaged envelope from 20 independent DAMMIF runs with DAMMIN (*60*).

suggesting that the tetrahedral domains assembled into a bipyramidal shape as designed (Fig. 5, G and H, and fig. S25). Moreover, theoretical scattering curves calculated for tetrahedral models of individual subunits or open conformations of the bipyramidal cage did not match the observed SAXS scattering curve (fig. S25). The molecular envelope obtained with an ab initio reconstruction from SAXS data overlapped reasonably well with the best-fit cage model (Fig. 5H and fig. S26). The slight deviation between the envelope and best-fit model might be due to the presence of an exposed central cavity, a characteristic feature of CCPO cages or the partial flexibility of the bipyramidal cage detected also in the Kratky plot (fig. S25).

DISCUSSION

One of the reasons the design of bridging metal centers has been such a successful strategy for generating supramolecular complexes is the relative strength of the metal-ligand bond driving the assembly, resulting in a robust design (*45*, *46*). However, the oligomerization state of the self-assembled structure does not depend only on the preferred coordination geometry of the metal ion but also on non-covalent interactions between residues that come in close proximity as a result of the metal ion–mediated assembly, rendering the design of supramolecular assemblies via metal coordination more difficult (*46*). By incorporating $ZnHis_3$, a frequently used motif in metalloprotein design, into an orthogonal CC set, we harnessed the importance of noncovalent interactions to design a set of four orthogonal Zn(II)-dependent heterodimeric CCs that differ in the pattern of electrostatic, hydrophobic, and metal chelating interactions.

While our modular design strategy highlights how metal sites can be used to guide CC self-assembly, the position of the binding site in the peptide sequence importantly affected the Zn(II)-dependent

self-assembly. Terminally positioned binding site did not provide a sufficient perturbation to the hydrophobic seam to prevent CC formation in the absence of metal ions, while placing the $ZnHis_3$ motif in the second or third heptad, located centrally, resulted in Zn(II)-controlled self-assembly. This suggests that the cluster of hydrophobic interactions is more potently disrupted at its center. CCs with the $ZnHis_3$ motif in the second heptad versus the third heptad behaved somewhat differently. α-Helical content was higher for CC pairs containing $ZnHis_3$ motif in the second heptad (62 and 66% for $CC56_{SHb}3H2$ and $CC78_{SHb}3H2$; Fig. 1, F and H, respectively) than if the binding site was present in the third heptad (55 and 50% for $CC34_{SHb}3H3$ and $CC56_{SHb}3H3$; Fig. 1, E and G, respectively). Conversely, thermal stability was lower if $ZnHis_3$ was positioned in the second heptad. In addition, peptide pairs that contained the binding site in the second heptad displayed a somewhat weaker Zn(II) binding affinity in comparison to peptide pairs with His residues in the third heptad. We posit that the Zn(II) coordination site to a certain degree represents a disruption in the CC motif. Consequently, this affects the balance between binding affinity and helical content, with more rigidly organized coordination sites leading to higher Zn(II) affinity and thermal stability, but less helical assemblies. It is possible that the position of the $ZnHis_3$ motif in the peptide sequence also affects the precise metal coordination geometry. High-resolution structural characterization of the peptides in complex with Zn(II) ions aimed at understanding the origins of these differences is ongoing.

Successfully designed peptide pairs displayed a high degree of orthogonality. Although $CC56_{SHb}3H2$ and $CC56_{SHb}3H3$ displayed some degree of cross-reactivity, on-target pairing was still preferred, even though the two peptide pairs shared the same hydrophobic and electrostatic pattern but differed in the position of the metal binding site. This suggests the possibility of combining standard CC noncovalent interactions with engineered metal sites to expand the size of available orthogonal CC pairs, allowing for the design of more complex CC-based nanostructures. However, insertion of several mutations in a CC pair can disrupt the pairing specificity imparted by the hydrophobic and electrostatic interaction pattern, as in the case of $CC56_{SHb}6H$.

To explore the potential of the developed CCs as building blocks for designing dynamic protein assemblies, the set was used to construct a series of CCPO polyhedral cages. The initially designed single-chain CCPO triangle composed of validated Zn(II)-responsive CCs ($CC78_{SHb}3H2$, $CC34_{SHb}3H3$, and $CC56_{SHb}3H3$) displayed Zn(II)-dependent folding only at elevated temperatures. This reflects the strong effect that connecting peptide pairs into a single chain has on the thermodynamics of the assembly by reducing the loss in entropy normally associated with dimerization. Because of the modular nature of CCPO cages, we were able to reduce the temperature range where Zn(II) ions controlled the folding equilibrium of the CCPO triangle by modulating its stability at the level of individual CC pairs. We demonstrated that several strategies can be used to manipulate the stability of the triangular fold: building block swapping, engineering of additional metal binding sites, or mutation of solvent exposed *b*, *c*, *f* residues. To achieve Zn(II)-induced folding of single-chain structures at room temperature, it was necessary to destabilize all the building modules. This highlights the strength of the CCPO design strategy, namely, that the properties of individual CC modules can be tuned in a wide range; however, the behavior of CCPO cages depends on the combination of selected CC modules and their cumulative contributions. Conversely, in the case of the CCPO bipyramid, adjusting the stability of the Zn(II)-responsive CC elements was not required.

Together, our results show the developed CC toolbox can be used to regulate the assembly of both multimeric and monomeric CCPO structures. The ability to reliably and reversibly control the quaternary structure of CC-based cages will facilitate the design of molecular machines for various applications, e.g., CC-based cages for delivery and release of cargo in cellular environments with low Zn(II) concentration or low pH [e.g., in the nucleus (*47*) or endosomes (*48*)]. In addition, because the N and C termini of CCPO cages come into close proximity in the folded state, Zn(II)-dependent CCPO triangles could be used to control the activity of split proteins, whose function requires interaction between separate protein halves, or as protein sensors of cellular Zn(II), where the ability to modulate Zn(II) affinity could be particularly advantageous. Last, we believe the developed set of CC conformational switches could also be used to program dynamic properties into other previously reported CC-based nanostructures (*9*, *11*, *49*) with minimal adaptation and likely also in other contexts with CC modules serving as the interaction interface. Because of their hetero-specificity, they are particularly suited for labeling applications and as scaffolds to govern intracellular trafficking, bring distinct protein domains in close proximity, for example, to create biocatalytic cascades, or perform information processing within cells (*50*).

MATERIALS AND METHODS

Materials

Chemicals were purchased from Sigma-Aldrich (Merck, Germany). The peptides were purchased from Proteogenix (France). The peptides' N termini were protected by the acetyl group, while the C termini were protected by amidation. Synthetic genes were ordered from Twist Bioscience (CA, USA).

Design and modeling of CCPO structures

Models of CC pairs were generated with ISAMBARD CC modeling package written in Python (*51*). Optimal structural parameters (superhelix radius, pitch, and Crick angle) were found with a genetic algorithm. BUDE force field was used to calculate the internal energy.

CCPO design strategy consists of covalently linking CC-forming peptides into a single polypeptide chain that can fold into the desired structure. For each new polyhedral shape, a topological analysis has to be performed to find all Eulerian double paths, i.e., paths that visit each polyhedral edge exactly twice, providing a blueprint for connecting the CC-forming peptides. In the case of two-dimensional objects such as triangles, the solution is trivial. There is a single possible double path, which circumvents the shape twice. After choosing the appropriate building blocks as described in the Results section, molecular models of CCPO triangles were built using the CoCoPOD computational platform (*16*) available at https://github.com/NIC-SBI/CC_protein_origami. CCPO bipyramid with Zn(II)-dependent assembly was designed on the basis of the previously reported bipyramidal cage $SBP12_{9,b}$ (*17*). The latter was composed from two tetrahedral domains interacting via a triangular interface, encompassing three CC pairs. To achieve Zn(II)-directed assembly, the interfacial peptides were exchanged for Zn(II)-responsive CC pairs. Bipyramid models were built using the CoCoPOD computational platform (*16*, *17*).

Molecular cloning

Passages of plasmid propagation were carried out using the *E. coli* strain DH5-α [F^- φ80*lac*ZΔM15 Δ(*lac*ZYA-*arg*F) U169 *rec*A1 *end*A1 *hsd*R17(r_K^-, m_K^+) *pho*A *sup*E44 λ^- *thi*-1 *gyr*A96 *rel*A1] (NEB, MA, USA). Transformation was carried out via heat shock with competent *E. coli* cells. Single colonies were propagated in the presence of the antibiotic kanamycin (Goldbio, MO, USA), added to Lysogeny broth (LB) media to reach 50 μg/ml.

All the proteins characterized in vitro were cloned in the expression vector pET41a(+) (Merck, Germany) between the restriction sites Nde I and Xho I. The affinity tags at either the 5′ or 3′ end were cloned between the restriction sites Xba I and Nde I or Xho I and Avr II, respectively. The DNA sequences coding for the protein constructs were optimized for *E. coli* codon usage and subsequently purchased from Twist Bioscience (CA, USA). DNA sequences were introduced in the expression vector either with Gibson assembly (*52*) or via restriction with enzymes Nde I and Xho I (NEB, MA, USA) and ligation with T4 ligase (NEB, MA, USA) according to the manufacturer's instructions. Gibson assembly was carried out with the enzymes Taq Ligase, Phusion Polymerase, and T5 exonuclease (NEB, MA, USA). DNA purification was carried out with Spin Miniprep Kit (QIAGEN, Germany).

Proteins TRI6-1b, TRI6-2, and TRI6-2b were cloned with a Strep-tag at their C-terminal end. Proteins TRI6-control, TRI6-1, TRI6-3, TRI6-4, TRI6-5, TRI6-6, $SBP^{Zn}1$, and $SBP^{Zn}2$ were required to be further purified and were, therefore, cloned with an additional His-tag at the N termini. A TEV protease cleavage site was introduced between the His-tag and the protein to allow for His-tag removal after affinity purification.

Protein production

E. coli strain NiCO21(DE3) (*53*) was used for producing all the proteins [*can::CBD fhuA2 [lon] ompT gal (λ DE3) [dcm] arnA::CBD slyD::CBD glmS6Ala ΔhsdS λ DE3 = λ sBamHIo ΔEco RI-B int::(lacI::PlacUV5::T7 gene1) i21 Δnin5*] (NEB, MA, USA). Bacteria were grown at 37°C in LB media supplemented with 50 μg/ml of kanamycin at 160 RPM overnight. The precultures were then diluted to 0.1 OD in 1 liter of LB media supplemented with kanamycin (50 μg/ml) and left growing at 37°C before reaching stationary phase. At OD values between 0.6 and 0.9, the cultures were induced with 1 mM isopropyl-β-D-thiogalactopyranoside (Goldbio, MO, USA) and grown for 4 hours in agitation (160 RPM) at 30°C.

At the end of the induction, the cells were resuspended in 12 ml per liter of culture of lysis buffer [50 mM tris-HCl (pH 8), 150 mM NaCl, 10 mM imidazole, Benzonase (0.06 μl/ml; Merck, Germany), 1 mM $MgCl_2$, CPI (2 μl/ml; Protease Inhibitor Cocktails, Millex Sigma-Aldrich, MO, USA), and 1 mM TCEP (Millex Sigma-Aldrich, MO, USA)]. Cell lysis was completed by ultrasonication with a Vibra-cell VCX (Sonics, CT, USA) on ice for a maximum of four cycles of 1 min of total pulse time, at intervals of 1-s pulse and 3-s pause (55% amplitude).

Alternatively, thermal lysis was applied for the proteins $SBP^{Zn}1$ and $SBP^{Zn}2$. Cells were resuspended in 20 ml per liter of culture of lysis buffer and incubated for 15 min at 95°C, subsequently cooled in ice, and supplemented with an additional aliquot of 0.06 μl/ml of Benzonase before centrifugation.

The cellular lysates were centrifuged at 16,000*g* for 20 min (4°C). The soluble fraction was then filtered through 0.45-μm filter units (Sartorius Stedim, Germany). After filtration, soluble fractions of bacterial lysates were flown though a 5-ml HisTrap HP (Cytiva, MA, USA) previously equilibrated with buffer A [50 mM tris-HCl (pH 8.0), 150 mM NaCl, 10 mM imidazole, and 1 mM TCEP]. After washing with buffer A, a gradient against buffer B [50 mM tris-HCl (pH 8.0), 150 mM NaCl, 500 mM imidazole, and 1 mM TCEP] was established.

TEV protease was produced following a standard protocol (*17*) and used to cleave the His-tag after the first affinity chromatography. Controlled proteolysis was performed overnight at 4°C with addition of 10 μg of TEV protease per 1 mg of target protein.

Strep-tag affinity was performed according to the manufacturer instructions with four StrepTrap HP 5-ml columns (Cytiva, MA, USA) connected in series and conditioned with buffer C [50 mM tris-HCl (pH 8.0), 150 mM NaCl, 1 mM EDTA, and 1 mM TCEP]. After binding and washing, the protein was eluted with 2.5 mM D-Desthiobiotin (Millex Sigma-Aldrich, MO, USA) dissolved in buffer C.

For SEC, we used HiLoad Superdex 200 resin (Cytiva, MA, USA), packed in a 26/600 XK column (Cytiva, MA, USA) equilibrated with filtered and degassed SEC buffer [20 mM tris-HCl (pH 7.5), 150 mM NaCl, 10% glycerol, v/v, and 1 mM TCEP]. Samples were injected into the column after concentration with centrifugal filters (3K or 10K; Amicon-ultra, Millex Sigma-Aldrich, MO, USA) and filtration in 0.22-μm syringe filters (Millex Sigma-Aldrich, MO, USA). The chromatography was run with an AKTA pure FPLC system (Cytiva, MA, USA) in SEC buffer with a linear flow rate of 2.6 ml/min.

To remove the residual uncleaved protein, the sample was flown through 2.5 ml of Ni-NTA resin (Goldbio, MO, USA) previously conditioned in buffer A and eluted with buffer D [50 mM tris-HCl (pH 8.0), 150 mM NaCl, 50 mM imidazole, and 1 mM TCEP]. Samples were analyzed by SDS–polyacrylamide gel electrophoresis (SDS-PAGE) (*54*) in a Bio-Rad (CA, USA) mini-PROTEAN apparatus in 12% or 15% discontinuous polyacrylamide gels containing SDS, next to prestained molecular markers (Thermo Fisher Scientific, MA, USA). Afterward, the gels were dyed with InstantBlue (Millex Sigma-Aldrich, MO, USA). SDS-PAGE confirmed the uncleaved protein remained bound to the Ni-NTA resin.

After the isolation process, any bound metal ions were removed with dialysis. First, EDTA was added to the samples to reach 5 mM final concentration. The sample was then dialysed against 1 liter of tris-based buffer (50 mM tris, 150 mM NaCl, and 1 mM TCEP at pH 7.5) containing 5 mM EDTA. The dialysis proceeded for at least 24 hours, with a buffer change after the first 6 hours. To remove EDTA, the dialysis procedure was repeated, but without including EDTA in the dialysis buffer (50 mM tris, 150 mM NaCl, and 1 mM TCEP at pH 7.5).

The proteins were stored at −80°C after being flash frozen in liquid nitrogen. Protein concentrations were determined measuring absorbance at 280 nm using the extinction coefficients calculated with ProtParam (*55*).

FRET experiments

Cysteine residues in selected protein constructs were fluorescently labeled with Sulfo-cy3 and Sulfo-cy5 (Lumiprobe, MD, USA) via thiol-maleimide coupling. Dyes were dissolved in 100 μM dimethyl sulfoxide to approximately 5 mM final concentration. Dyes were added to 1 ml of protein solution at 1 mg/ml in 10-fold molar excess. $SBP^{Zn}1$ was labeled with Sulfo-cy3, while $SBP^{Zn}2$ was labeled

with Sulfo-cy5. In the case of triangular designs, the dyes were first mixed together and then added to the protein solution. The reaction mixture was left overnight at 4°C. The labeled proteins were purified on PD 10 disposable desalting column (Cytiva, MA, USA) with tris buffer (50 mM tris and 150 mM NaCl, pH 7) used as the mobile phase.

Fluorescents spectra were measured with multiplate fluorescence reader Synergy Mx (Bio TeK, VT, USA) in 96-well plates. For triangular constructs, 80 μl of protein solution (6.25 μM) was placed in each well. Stock $ZnCl_2$ solution (30 mM $ZnCl_2$, 50 mM tris, and 150 mM NaCl, pH 6) was added to the wells to reach target Zn(II) concentration. Sample volume was adjusted to 100 μl by addition of tris buffer. For the complex $SBP^{Zn}1$:$SBP^{Zn}2$, the proteins were mixed in equimolar ratio in a final volume of 50 or 100 μl in 96-well plates at a final concentration of 1.5 μM. The protein was titrated with $ZnCl_2$ or other metals in a range of concentrations between 0.1 and 7 μM. Three independent samples were measured for each concentration. FRET ratio was calculated as

$$\text{FRET} = \frac{I_A}{I_A + I_D}$$

where I_A is acceptor emission at 668 nm, and I_D is the donor emission at 563 nm upon excitation at 528 nm. The model fitting was performed with Python package SciPy (*56*) and is described in detail in the Supplementary Materials.

CD spectroscopy

CD experiments were performed on a ChiraScan instrument (Applied Photophysics, UK). Temperature was controlled with a Peltier thermal control block (Melcor, NJ, USA, now part of Laird Technologies). For individual peptides and CC peptide pairs, CD measurements were performed at 20 μM concentration. Samples of CCPO triangles were measured at approximately 6 μM concentration. The proteins $SBP^{Zn}1$ and $SBP^{Zn}2$ were measured at a concentration of approximately 10 μM. Samples were placed in a 1-mm quartz cuvette, and ellipticity was measured between 200 and 280 nm with a 1-nm step size, 1-nm bandwidth, and 0.5 integration time. Each spectrum was recorded three times. Helical content was calculated from mean residue ellipticity at 222 nm (MRE_{222}) as (*57*)

$$\text{Helical content}(\%) = \frac{\text{MRE}_{222}}{\text{MRE}^{H}_{222} \times \left(1 - \frac{2.57}{n}\right)}$$

where n is the length of the amino acid sequence, and MRE^{H}_{222} is the theoretical mean residue ellipticity of an infinitely long helix (−39,500 deg cm^2 $dmol^{-1}$) (*57*).

To compare the binding affinities of selected divalent metal ions for CC peptides and CCPO triangles, CD titration experiments were performed. Stock solutions of metal ions (30 mM $ZnCl_2$ at pH 6, 30 mM $NiCl_2$ at pH 7, 30 mM $CoCl_2$ at pH 7, and 30 mM $CuCl_2$ at pH 7) in tris buffer (50 mM tris and 150 mM NaCl) were incrementally added to peptide or protein solutions, and CD spectra were recorded after each addition. Thermodynamic analysis of the obtained binding isotherms is described in the Supplementary Materials.

Thermal stability was evaluated by following MRE_{222} as a function of temperature in the presence and absence of Zn(II) ions. The temperature was increased from 4° to 90°C at a rate of 1°C/min with ellipticity measured at 1°C increments. The effective temperature was recorded using a temperature probe placed inside the cuvette. T_ms were determined by fitting a thermodynamic model to experimental CD data as described in the Supplementary Materials.

Size exclusion chromatography coupled to light scattering

SEC-MALS analysis was conducted with a high-performance liquid chromatography system (Waters, MA, USA), coupled to a ultraviolet detector, a Dawn8+ multiple-angle light scattering detector (Wyatt, CA, USA), and a refractive index detector RI500 (Shodex, Japan). Dissolved peptides were filtered through Durapore 0.1-μm centrifuge filters (Millex Sigma-Aldrich, MO, USA) and applied either to a Biosep S2000 SEC 300 × 7.8 column (Phenomenex, CA, USA) in tris buffer (50 mM tris at pH 7.5, 150 mM NaCl, and 1 mM TCEP) or to a Superdex 75 increase 10/300 column (Cytiva, MA, USA) in tris buffer supplemented with 100 μM $ZnCl_2$. Protein samples were filtered through Durapore 0.1-μm centrifuge filters and applied either to a Superdex 75 increase 10/300 column (Cytiva, MA, USA) or to a Superdex 200 increase 10/300 column (Cytiva, MA, USA) equilibrated in Hepes buffer (50 mM Hepes at pH 8, 150 mM NaCl, and 1 mM TCEP) with or without $ZnCl_2$. The triangular proteins were injected at a concentration of approximatively 1 mg/ml, while the proteins $SBP^{Zn}1$ and $SBP^{Zn}2$ were injected at a concentration of approximately 0.5 mg/ml. Accordingly, a different concentration of $ZnCl_2$ was added to the mobile phase, 500 μM for triangular proteins and 20 μM for proteins $SBP^{Zn}1$ and $SBP^{Zn}2$. Analysis of the peaks of interest was conducted with Astra 7.0 software (Wyatt, CA, USA).

Small-angle x-ray scattering

SAXS experiments were performed at the P12 beamline that is part of the PETRA-III synchrotron (DESY, Hamburg, Germany). To avoid absorption by Zn(II), x-ray wavelength was 1.38 Å. Scattering intensity was recorded in the range from 0.028 to 6.6 nm^{-1} with the Pilatus 6M detector, placed 3 m from the sample. Batch measurements were performed with the robotic sample handler (*58*) in flow-through mode to avoid radiation damage. Sample volume was 40 μl. Buffer scattering was collected before and after each sample and used for background subtraction. For each sample and buffer, scattering was recorded over 40 frames lasting 0.05 s. Frames without any radiation damage were automatically averaged (*59*). To determine the structure of CCPO triangles in the absence of Zn(II) ions, a dilution series consisting of at least four concentrations (~1, 2, 4, and 8 mg/ml) was prepared and measured for each protein variant. In addition, scattering was recorded at different Zn(II) concentrations (0, 30, 100, 300, and 500 μM). Before SAXS measurements, 100 μl of protein sample (1 mg/ml) was dialyzed against 1 liter of Hepes-based buffer (50 mM Hepes, 150 mM NaCl, 1 mM TCEP, and 10% glycerol, pH 7) at target $ZnCl_2$ concentration. The structure of the complex $SBP^{Zn}1$:$SBP^{Zn}2$ was analyzed with SEC-SAXS. Mobile phase (50 mM Hepes, 150 mM NaCl, 1 mM TCEP, 100 μM $ZnCl_2$, and 10% glycerol, pH 7.5) was flown through the column (Superdex 200 increase 10/300; GE Healthcare, IL, USA) at a flow of 0.4 ml/min. A total of 3600 scattering frames were collected with exposure time of 0.995 s. ATSAS software (*60*) was used for merging and data analysis. Ab initio modeling of molecular envelopes was performed in two steps. First, 20 structures were generated with DAMMIF and were subsequently averaged with DAMAVER. The averaged model was lastly refined with DAMMIN. PepsiSAXS (*61*) was used to compare experimental scattering profiles to model structures generated with the CoCoPOD software.

EOM 2.0 was used to analyze the conformational flexibility of triangular constructs in the absence of Zn(II) ions. A total of 10,000 random chain configurations were generated, and genetic algorithm was run 50 times to obtain a good ensemble fit. The pool of partially folded triangular structures, differing in the number of assembled CC pairs, was generated with the CoCoPOD software. Because the unpaired peptides likely do not have helical secondary structure, the models were subjected to a short molecular dynamics (MD) optimization, run at an elevated temperature (500 K) to unfold the unpaired peptides. The assembled CCs were treated as rigid bodies. Models both before and after MD optimization, totaling 210 structures, were fit to experimental scattering profiles to identify a single best matching structure.

SUPPLEMENTARY MATERIALS

Supplementary material for this article is available at https://science.org/doi/10.1126/sciadv.abm8243

View/request a protocol for this paper from *Bio-protocol*.

REFERENCES AND NOTES

1. T. Blundell, G. Dodson, D. Hodgkin, D. Mercola, Insulin: The structure in the crystal and its reflection in chemistry and biology. *Adv. Protein Chem.* **26**, 279–286 (1972).
2. B. C. Cunningham, M. G. Mulkerrin, J. A. Wells, Dimerization of human growth hormone by zinc. *Science* **253**, 545–548 (1991).
3. A. G. Szent-Györgyi, Calcium regulation of muscle contraction. *Biophys. J.* **15**, 707–723 (1975).
4. P. A. Davies, W. Wang, T. G. Hales, E. F. Kirkness, A novel class of ligand-gated ion channel is activated by Zn^{2+}. *J. Biol. Chem.* **278**, 712–717 (2003).
5. J. H. Shin, H. J. Jung, Y. J. An, Y. B. Cho, S. S. Cha, J. H. Roe, Graded expression of zinc-responsive genes through two regulatory zinc-binding sites in Zur. *Proc. Natl. Acad. Sci. U.S.A.* **108**, 5045–5050 (2011).
6. W. Qiao, M. Mooney, A. J. Bird, D. R. Winge, D. J. Eide, Zinc binding to a regulatory zinc-sensing domain monitored in vivo by using FRET. *Proc. Natl. Acad. Sci. U.S.A.* **103**, 8674–8679 (2006).
7. C. Eicken, M. A. Pennella, X. Chen, K. M. Koshlap, M. L. VanZile, J. C. Sacchettini, D. P. Giedroc, A metal-ligand-mediated intersubunit allosteric switch in related SmtB/ArsR zinc sensor proteins. *J. Mol. Biol.* **333**, 683–695 (2003).
8. M. McMahon, S. R. Swift, J. D. Hayes, Zinc-binding triggers a conformational-switch in the cullin-3 substrate adaptor protein KEAP1 that controls transcription factor NRF2. *Toxicol. Appl. Pharmacol.* **360**, 45–57 (2018).
9. J. M. Fletcher, R. L. Harniman, F. R. H. Barnes, A. L. Boyle, A. Collins, J. Mantell, T. H. Sharp, M. Antognozzi, P. J. Booth, N. Linden, M. J. Miles, R. B. Sessions, P. Verkade, D. N. Woolfson, Self-assembling cages from coiled-coil peptide modules. *Science* **340**, 595–599 (2013).
10. Z. Chen, M. C. Johnson, J. Chen, M. J. Bick, S. E. Boyken, B. Lin, J. J. de Yoreo, J. M. Kollman, D. Baker, F. DiMaio, Self-assembling 2D arrays with de novo protein building blocks. *J. Am. Chem. Soc.* **141**, 8891–8895 (2019).
11. J. P. M. Vrancken, J. P. M. Vrancken, J. Aupič, C. Addy, R. Jerala, J. R. H. Tame, A. R. D. Voet, Molecular assemblies built with the artificial protein Pizza. *J. Struct. Biol. X* **4**, 100027 (2020).
12. D. N. Woolfson, The design of coiled-coil structures and assemblies. *Adv. Protein Chem.* **70**, 79–112 (2005).
13. I. Drobnak, H. Gradišar, A. Ljubetič, E. Merljak, R. Jerala, Modulation of coiled-coil dimer stability through surface residues while preserving pairing specificity. *J. Am. Chem. Soc.* **139**, 8229–8236 (2017).
14. D. N. Woolfson, Coiled-coil design: Updated and upgraded. *Subcell. Biochem.* **82**, 35–61 (2017).
15. H. Gradišar, S. Božič, T. Doles, D. Vengust, I. Hafner-Bratkovič, A. Mertelj, B. Webb, A. Šali, S. Klavžar, R. Jerala, Design of a single-chain polypeptide tetrahedron assembled from coiled-coil segments. *Nat. Chem. Biol.* **9**, 362–366 (2013).
16. A. Ljubetič, F. Lapenta, H. Gradišar, I. Drobnak, J. Aupič, Ž. Strmšek, D. Lainšček, I. Hafner-Bratkovič, A. Majerle, N. Krivec, M. Benčina, T. Pisanski, T. Ć. Veličković, A. Round, J. M. Carazo, R. Melero, R. Jerala, Design of coiled-coil protein-origami cages that self-assemble in vitro and in vivo. *Nat. Biotechnol.* **35**, 1094–1101 (2017).
17. F. Lapenta, J. Aupič, M. Vezzoli, Ž. Strmšek, S. D. Vela, D. I. Svergun, J. M. Carazo, R. Melero, R. Jerala, Self-assembly and regulation of protein cages from pre-organised coiled-coil modules. *Nat. Commun.* **12**, 939 (2021).
18. W. M. Park, M. Bedewy, K. K. Berggren, A. E. Keating, Modular assembly of a protein nanotriangle using orthogonally interacting coiled coils. *Sci. Rep.* **7**, 10577 (2017).
19. S. Božič Abram, H. Gradišar, J. Aupič, A. R. Round, R. Jerala, Triangular in vivo self-assembling coiled-coil protein origami. *ACS Chem. Biol.* **16**, 310–315 (2021).
20. H. Gradišar, R. Jerala, De novo design of orthogonal peptide pairs forming parallel coiled-coil heterodimers. *J. Pept. Sci.* **17**, 100–106 (2011).
21. T. Handel, W. F. DeGrado, De novo design of a Zn^{2+}-binding protein. *J. Am. Chem. Soc.* **112**, 6710–6711 (1990).
22. T. M. Handel, S. A. Williams, W. F. DeGrado, Metal ion-dependent modulation of the dynamics of a designed protein. *Science* **261**, 879–885 (1993).
23. M. L. Zastrow, V. L. Pecoraro, Designing functional metalloproteins: From structural to catalytic metal sites. *Coord. Chem. Rev.* **257**, 2565–2588 (2013).
24. G. R. Dieckmann, D. K. McRorie, D. L. Tierney, L. M. Utschig, C. P. Singer, T. V. O'Halloran, J. E. Penner-Hahn, W. F. DeGrado, V. L. Pecoraro, De novo design of mercury-binding two- and three-helical bundles. *J. Am. Chem. Soc.* **119**, 6195–6196 (1997).
25. M. R. Berwick, D. J. Lewis, A. W. Jones, R. A. Parslow, T. R. Dafforn, H. J. Cooper, J. Wilkie, Z. Pikramenou, M. M. Britton, A. F. A. Peacock, De novo design of Ln(III) coiled coils for imaging applications. *J. Am. Chem. Soc.* **136**, 1166–1169 (2014).
26. N. H. Joh, T. Wang, M. P. Bhate, R. Acharya, Y. Wu, M. Grabe, M. Hong, G. Grigoryan, W. F. DeGrado, De novo design of a transmembrane Zn^{2+}-transporting four-helix bundle. *Science* **346**, 1520–1524 (2014).
27. G. R. Dieckmann, D. K. McRorie, J. D. Lear, K. A. Sharp, W. F. DeGrado, V. L. Pecoraro, The role of protonation and metal chelation preferences in defining the properties of mercury-binding coiled coils. *J. Mol. Biol.* **280**, 897–912 (1998).
28. T. Tanaka, T. Mizuno, S. Fukui, H. Hiroaki, J. I. Oku, K. Kanaori, K. Tajima, M. Shirakawa, Two-metal ion, Ni(II) and Cu(II), binding α-helical coiled coil peptide. *J. Am. Chem. Soc.* **126**, 14023–14028 (2004).
29. P. Teare, C. F. Smith, S. J. Adams, S. Anbu, B. Ciani, L. J. C. Jeuken, A. F. A. Peacock, pH dependent binding in de novo hetero bimetallic coiled coils. *Dalton Trans.* **47**, 10784–10790 (2018).
30. B. S. Der, M. Machius, M. J. Miley, J. L. Mills, T. Szyperski, B. Kuhlman, Metal-mediated affinity and orientation specificity in a computationally designed protein homodimer. *J. Am. Chem. Soc.* **134**, 375–385 (2012).
31. A. Pasternak, J. Kaplan, J. D. Lear, W. F. Degrado, Proton and metal ion-dependent assembly of a model diiron protein. *Protein Sci.* **10**, 958–969 (2001).
32. E. N. G. Marsh, W. F. Degrado, Noncovalent self-assembly of a heterotetrameric diiron protein. *Proc. Natl. Acad. Sci. U.S.A.* **99**, 5150–5154 (2002).
33. A. L. Boyle, M. Rabe, N. S. A. Crone, G. G. Rhys, N. Soler, P. Voskamp, N. S. Pannu, A. Kros, Selective coordination of three transition metal ions within a coiled-coil peptide scaffold. *Chem. Sci.* **10**, 7456–7465 (2019).
34. J. Aupič, F. Lapenta, R. Jerala, SwitCCh: Metal-site design for controlling the assembly of a coiled-coil homodimer. *Chembiochem* **19**, 2453–2457 (2018).
35. K. Suzuki, H. Hiroaki, D. Kohda, H. Nakamura, T. Tanaka, Metal ion induced self-assembly of a designed peptide into a triple-stranded α-helical bundle: A novel metal binding site in the hydrophobic core. *J. Am. Chem. Soc.* **120**, 13008–13015 (1998).
36. O. A. Kharenko, M. Y. Ogawa, Metal-induced folding of a designed metalloprotein. *J. Inorg. Biochem.* **98**, 1971–1974 (2004).
37. W. D. Kohn, C. M. Kay, B. D. Sykes, R. S. Hodges, Metal ion induced folding of a de novo designed coiled-coil peptide. *J. Am. Chem. Soc.* **120**, 1124–1132 (1998).
38. E. Golub, R. H. Subramanian, J. Esselborn, R. G. Alberstein, J. B. Bailey, J. A. Chiong, X. Yan, T. Booth, T. S. Baker, F. A. Tezcan, Constructing protein polyhedra via orthogonal chemical interactions. *Nature* **578**, 172–176 (2020).
39. F. Lapenta, J. Aupič, Ž. Strmšek, R. Jerala, Coiled coil protein origami: From modular design principles towards biotechnological applications. *Chem. Soc. Rev.* **47**, 3530–3542 (2018).
40. H. Sigel, *Metal Ions in Biological Systems: Volume 15: Zinc and Its Role in Biology and Nutrition* (CRC press, 1983), vol. 15.
41. M. M. Harding, Geometry of metal-ligand interactions in proteins. *Acta Crystallogr. D Biol. Crystallogr.* **57**, 401–411 (2001).
42. S. Dutta, D. Bhattacharyya, Size of unfolded and dissociated subunits versus that of native multimeric proteins. *J. Biol. Phys.* **27**, 59–71 (2001).
43. G. Tria, H. D. T. Mertens, M. Kachala, D. I. Svergun, Advanced ensemble modelling of flexible macromolecules using x-ray solution scattering. *IUCrJ.* **2**, 207–217 (2015).
44. V. M. Burger, D. J. Arenas, C. M. Stultz, A structure-free method for quantifying conformational flexibility in proteins. *Sci. Rep.* **6**, 29040 (2016).
45. E. N. Salgado, X. I. Ambroggio, J. D. Brodin, R. A. Lewis, B. Kuhlman, F. A. Tezcan, Metal templated design of protein interfaces. *Proc. Natl. Acad. Sci. U.S.A.* **107**, 1827–1832 (2010).
46. E. N. Salgado, R. J. Radford, F. A. Tezcan, Metal-directed protein self-assembly. *Acc. Chem. Res.* **43**, 661–672 (2010).
47. Q. Lu, H. Haragopal, K. G. Slepchenko, C. Stork, Y. V. Li, Intracellular zinc distribution in mitochondria, ER and the Golgi apparatus. *Int. J. Physiol. Pathophysiol. Pharmacol.* **8**, 35–43 (2016).

48. J. R. Casey, S. Grinstein, J. Orlowski, Sensors and regulators of intracellular pH. *Nat. Rev. Mol. Cell Biol.* **11**, 50–61 (2010).
49. E. De Santis, M. G. Ryadnov, Peptide self-assembly for nanomaterials: The old new kid on the block. *Chem. Soc. Rev.* **44**, 8288–8300 (2015).
50. T. Fink, J. Lonzarić, A. Praznik, T. Plaper, E. Merljak, K. Leben, N. Jerala, T. Lebar, Ž. Strmšek, F. Lapenta, M. Benčina, R. Jerala, Design of fast proteolysis-based signaling and logic circuits in mammalian cells. *Nat. Chem. Biol.* **15**, 115–122 (2019).
51. C. W. Wood, J. W. Heal, A. R. Thomson, G. J. Bartlett, A. Á. Ibarra, R. L. Brady, R. B. Sessions, D. N. Woolfson, ISAMBARD: An open-source computational environment for biomolecular analysis, modelling and design. *Bioinformatics* **33**, 3043–3050 (2017).
52. D. G. Gibson, L. Young, R. Y. Chuang, J. C. Venter, C. A. Hutchison III, H. O. Smith, Enzymatic assembly of DNA molecules up to several hundred kilobases. *Nat. Methods* **6**, 343–345 (2009).
53. C. Robichon, J. Luo, T. B. Causey, J. S. Benner, J. C. Samuelson, Engineering Escherichia coli BL21(DE3) derivative strains to minimize E. coli protein contamination after purification by immobilized metal affinity chromatography. *Appl. Environ. Microbiol.* **77**, 4634–4646 (2011).
54. U. K. Laemmli, Cleavage of structural proteins during the assembly of the head of bacteriophage T4. *Nature* **227**, 680–685 (1970).
55. M. R. Wilkins, E. Gasteiger, A. Bairoch, J. C. Sanchez, K. L. Williams, R. D. Appel, D. F. Hochstrasser, Protein identification and analysis tools in the ExPASy server. *Methods Mol. Biol.* **112**, 531–552 (1999).
56. P. Virtanen, R. Gommers, T. E. Oliphant, M. Haberland, T. Reddy, D. Cournapeau, E. Burovski, P. Peterson, W. Weckesser, J. Bright, S. J. van der Walt, M. Brett, J. Wilson, K. J. Millman, N. Mayorov, A. R. J. Nelson, E. Jones, R. Kern, E. Larson, C. J. Carey, İ. Polat, Y. Feng, E. W. Moore, J. V. Plas, D. Laxalde, J. Perktold, R. Cimrman, I. Henriksen, E. A. Quintero, C. R. Harris, A. M. Archibald, A. H. Ribeiro, F. Pedregosa, P. van Mulbregt; SciPy 1.0 Contributors, SciPy 1.0: Fundamental algorithms for scientific computing in Python. *Nat. Methods* **17**, 261–272 (2020).
57. Y. H. Chen, J. T. Yang, K. H. Chau, Determination of the helix and β form of proteins in aqueous solution by circular dichroism. *Biochemistry* **13**, 3350–3359 (1974).
58. A. Round, F. Felisaz, L. Fodinger, A. Gobbo, J. Huet, C. Villard, C. E. Blanchet, P. Pernot, S. McSweeney, M. Roessle, D. I. Svergun, F. Cipriani, BioSAXS Sample Changer: A robotic sample changer for rapid and reliable high-throughput x-ray solution scattering experiments. *Acta Crystallogr. D Struct. Biol.* **71**, 67–75 (2015).
59. D. Franke, A. G. Kikhney, D. I. Svergun, Automated acquisition and analysis of small angle x-ray scattering data. *Nucl. Instrum. Methods Phys. Res. A* **689**, 52–59 (2012).
60. D. Franke, M. V. Petoukhov, P. V. Konarev, A. Panjkovich, A. Tuukkanen, H. D. T. Mertens, A. G. Kikhney, N. R. Hajizadeh, J. M. Franklin, C. M. Jeffries, D. I. Svergun, *ATSAS 2.8*: A comprehensive data analysis suite for small-angle scattering from macromolecular solutions. *J. Appl. Cryst.* **50**, 1212–1225 (2017).
61. S. Grudinin, M. Garkavenko, A. Kazennov, *Pepsi-SAXS*: An adaptive method for rapid and accurate computation of small-angle x-ray scattering profiles. *Acta Crystallogr. D Struct. Biol.* **73**, 449–464 (2017).
62. J. A. Nelder, R. Mead, A simplex method for function minimization. *Comput. J.* **7**, 308–313 (1965).
63. C. Zhu, R. H. Byrd, P. Lu, J. Nocedal, Algorithm 778: L-BFGS-B: Fortran subroutines for large-scale bound-constrained optimization. *ACM Trans. Math. Softw.* **23**, 550–560 (1997).
64. E. F. Pettersen, T. D. Goddard, C. C. Huang, G. S. Couch, D. M. Greenblatt, E. C. Meng, T. E. Ferrin, UCSF Chimera—A visualization system for exploratory research and analysis. *J. Comput. Chem.* **25**, 1605–1612 (2004).

Acknowledgments: The synchrotron SAXS data were collected at beamline P12 operated by EMBL Hamburg at the PETRA III storage ring (DESY, Hamburg, Germany). We would like to thank S. Da Vela for the assistance in using the beamline. **Funding:** This research was supported by Slovenian Research Agency projects P4-0176, J1-2481, J1-1711, J1-2481, and J1-9173, European Research Council (ERC) Advanced Grant project MaCChines grant agreement ID: 899259 (R.J.), iNEXT, grant number 653706 (PID: 2437, 2706), and ONR, grant number N62909-20-1-2090. **Author contributions:** Conceptualization: J.A., F.L., and R.J. Methodology: J.A., F.L., Ž.S., E.M., and T.P. Investigation: J.A., F.L., Ž.S., E.M., and T.P. Visualization: J.A. Supervision: R.J. Writing—original draft: J.A. and R.J. Writing—review and editing: J.A., F.L., Ž.S., E.M., T.P., and R.J. **Competing interests:** The authors declare that they have no competing interests. **Data and materials availability:** All data needed to evaluate the conclusions in the paper are present in the paper and/or the Supplementary Materials.

Submitted 14 October 2021
Accepted 4 May 2022
Published 17 June 2022
10.1126/sciadv.abm8243